

## Article

# The Application of Optical Sensors with Built-in Anchor-like Cavities in the Detection of Hemoglobin Concentration

Wen Jiang<sup>1,2,3</sup>, Shubin Yan<sup>2,3,\*</sup> , Yiru Su<sup>2</sup>, Chong Wang<sup>2,3</sup>, Taiquan Wu<sup>2,3</sup>, Yang Cui<sup>2,3</sup>, Chuanhui Zhu<sup>2,3</sup> , Yi Zhang<sup>2,3</sup>, Xiangyang Mu<sup>1</sup> and Guowang Gao<sup>1</sup>

<sup>1</sup> School of Electrical Engineering, Xi'an Shiyou University, Xi'an 710065, China; 22212030531@stumail.xsyu.edu.cn (W.J.); muyou98@xsyu.edu.cn (X.M.); wwgao@xsyu.edu.cn (G.G.)

<sup>2</sup> School of Electrical Engineering, Zhejiang University of Water Resources and Electric Power, Hangzhou 310018, China; 2022b03001@stu.zjweu.edu.cn (Y.S.); wangchong@zjweu.edu.cn (C.W.); wutq@zjweu.edu.cn (T.W.); cuiy@zjweu.edu.cn (Y.C.); zhchh@zjweu.edu.cn (C.Z.); zhangyi@zjweu.edu.cn (Y.Z.)

<sup>3</sup> Zhejiang-Belarus Joint Laboratory of Intelligent Equipment and System for Water Conservancy and Hydropower Safety Monitoring, Hangzhou 310018, China

\* Correspondence: yanshb@zjweu.edu.cn; Tel.: +86-186-3611-2255

**Abstract:** This paper introduces a refractive index sensor based on Fano resonance, utilizing a metal–insulator–metal (MIM) waveguide structure with an Anchor-like cavity. This study utilizes the finite element method (FEM) for analyzing the propagation characteristics of the structure. The evaluation concentrated on assessing how the refractive index and the structure's geometric parameters affect its sensing characteristics. The designed structure demonstrates optimum performance, achieving a maximum sensitivity of 2440 nm/RIU and an FOM of 63. Given its high sensitivity, this nanoscale refractive index sensor is ideal for detecting hemoglobin concentrations in blood, and the sensor's sensitivity is 0.6 nm·g/L, aiding in clinical prevention and treatment.

**Keywords:** refractive index sensor; MIM; Fano resonance; concentration detection



**Citation:** Jiang, W.; Yan, S.; Su, Y.; Wang, C.; Wu, T.; Cui, Y.; Zhu, C.; Zhang, Y.; Mu, X.; Gao, G. The Application of Optical Sensors with Built-in Anchor-like Cavities in the Detection of Hemoglobin Concentration. *Photonics* **2024**, *11*, 402. <https://doi.org/10.3390/photonics11050402>

Received: 26 March 2024

Revised: 17 April 2024

Accepted: 23 April 2024

Published: 26 April 2024



**Copyright:** © 2024 by the authors. Licensee MDPI, Basel, Switzerland. This article is an open access article distributed under the terms and conditions of the Creative Commons Attribution (CC BY) license (<https://creativecommons.org/licenses/by/4.0/>).

## 1. Introduction

Common optical refractive index sensors include optical fiber optic sensors [1], micro-ring resonator sensors [2], photonic crystal sensors [3], and surface plasmon resonance (SPR) sensors. Photonic devices excel over electronic devices in operating bandwidth; however, their miniaturization and integration are constrained by the optical diffraction limit, which in turn limits the development of optical refractive index sensor sizes [4]. However, surface plasmon polaritons (SPPs) are capable of exceeding the diffraction limit and can precisely manipulate light on the nanoscale [5]. Consequently, an increasing number of scholars are focusing on SPPs.

Surface plasmon polaritons (SPPs) are electromagnetic waves formed by the intricate interplay between the free electrons of the metal and incident photons [6], enabling the over-coming of diffraction limits and allowing for the precise manipulation of light at the nanoscale [7]. Therefore, SPPs have immense promise for applications in integrated optical circuits and subwavelength photonic devices, ushering in a new era of transformative possibilities in nanophotonics. This electromagnetic wave can propagate across the interfaces and confine the field energy to a small region around the interfaces, resulting in a rapid decrease in intensity in the direction perpendicular to the interfaces [8]. SPP (surface plasmon polariton) waveguides provide significant advantages in photonics, chiefly through their ability to overcome the physical limitations of the diffraction limit that constrain conventional dielectric waveguides. This property enables the control and manipulation of light at sub-wavelength dimensions, thus facilitating the development of ultra-compact and highly efficient photonic devices. Due to their unmatched nanoscale light manipulation

capabilities, SPPs are at the forefront of next-generation photonic technology, serving as the cornerstone for developing highly integrated chip-scale photonic devices. In addition, the potential for the seamless integration of SPPs with existing semiconductor platforms heralds new possibilities for advancements in optical computing and communications, positioning them as key innovations in optoelectronics and nanotechnology [9,10].

Surface plasmon excitations markedly enhance the electromagnetic field at the metal–dielectric interface, a phenomenon of critical importance for optical sensing and information processing. Firstly, the composite structure of micro- and nanomaterials reacts to these excitations through optical nonlinear effects, rendering the system highly sensitive to the local structure of the metal surface and to refractive index changes in the medium. This sensitivity not only aids in detecting changes in the surface morphology and refractive index but also enables the fabrication of devices such as surface plasmon resonance sensors [11–13], all-optical switches [14], and optical modulators [15]. These devices find widespread use in various fields, including biomolecular detection, chemical analysis, environmental monitoring, and optical communication, offering key technologies for optical sensing, super-resolution imaging, and information processing and transmission. These functions are crucial in the fields of nanophotonics, optical sensing, photonic chips, and surface-enhanced spectroscopy and serve as the foundation for developing novel nanophotonic devices, underscoring their significant application value in modern optoelectronics [16].

Surface plasmon polaritons (SPPs) can not only be generated at metal–dielectric interfaces but can also be excited through various waveguide structures, including metal–dielectric–metal (MIM) [17], dielectric–metal–dielectric [18], and dielectric–dielectric–metal [19] waveguides. In particular, MIM waveguides have attracted attention due to their excellent SPP confinement, low ohmic losses, and long transmission distances [20]. These waveguide systems can be designed with various structures to tune broadband and narrowband modes, achieving precise control of Fano resonances. Traditional MIM waveguide structures typically include straight waveguides and circular resonators to produce Fano resonances, but this method has certain performance limitations. Research has found that introducing defects into waveguides or resonators can effectively induce Fano resonances by disrupting propagation symmetry, enhancing performance. For example, by introducing a conical defect in a circular resonator, Rahmatiyar developed a new design for a nanoscale refractive index sensor, combining a ring resonator with an MIM waveguide [21]. Further research explored plasmonic systems with defective silver nanoribbons, discovering that these systems can produce two Fano resonances. In these systems, quadrupole modes, which are not directly excitable on complete nanoribbons, become feasible through the introduction of defects. These defective silver nanoribbons support super radiant dipole and quadrupole modes, thereby producing two asymmetric Fano tilts in the transmission spectrum [22]. Fei Hu’s work further demonstrated how adjusting the geometric parameters of silver nanorod defects, such as radius and the height or base length of an isosceles triangle resonator, can independently adjust the shape of the Fano resonances. These studies highlight the importance and potential of structural defects in designing nanophotonic devices with specific optical properties [23].

Additionally, Yang and colleagues proposed a metal–insulator–metal (MIM) waveguide structure that includes a cross-shaped cavity and baffles. This structure achieved a sensitivity of 1075 nm/RIU [24]. Wang and colleagues developed a structure that couples a metal–insulator–metal (MIM) waveguide with a semicircular cavity and two silver baffles, reaching a maximum sensitivity of 2200 nm/RIU [25]. Pang and his team designed a novel structure using an MIM waveguide and an oblique rectangular cavity [26]. Zhou presents a waveguide design incorporating two short stub resonators and a ring resonator. It achieves a peak sensitivity of 1650 nm/RIU and a figure of merit (FOM) of 117.8 [27]. Tathif reported a sensor composed of a straight waveguide, a groove, and a square ring resonator (SRR), with a maximum sensitivity of 1074.88 nm/RIU and a quality factor of 32.4 [28]. Tang and colleagues proposed a sensor with a sensitivity of 1125 nm/RIU [29]. Chen designed a structure with a semi-elliptical and rectangular ring resonator, achieving

an optimal sensitivity of 1384 nm/RIU and a quality factor of 28.4 [30]. This study proposes and investigates a new structure of a nanoscale refractive index sensor utilizing MIM waveguides, composed of an MIM bus waveguide and an internal Anchor-like resonator. It features relatively high sensitivity and quality factors, and the structure is simple, with a relatively small cavity area and low loss. Subsequently, we modified various structural parameters and the refractive index, observed changes in the transmission spectrum, and analyzed the impact on system sensing performance using the finite element method (FEM). Finally, it was applied in detecting hemoglobin concentrations in blood, and the sensor's sensitivity was 0.6 nm·g/L, providing a theoretical basis for the field of nanomedicine.

## 2. Materials and Methods

This study utilized the finite element method to examine the relationship between the Fano resonance and changes in refractive index. We observed how the resonance frequency and intensity changed with the refractive index and analyzed the magnetic field distribution. By adjusting the structure's geometrical parameters, including size and shape, we investigated their effects on Fano resonance. Given that the designed structure's thickness is negligible compared to the spp surface depth, simulating the 3D structure requires more demanding hardware configuration and meshing. However, as the magnetic field characteristics of the 3D structure are largely similar to those of the 2D structure, we opted for the 2D model for simplicity in calculations [31]. Figure 1 illustrates a 2D schematic of the symmetrical sensor structure along the centerline. As illustrated in Figure 1, the system was modeled in COMSOL, with the Anchor-like structure comprising a circle, a rectangular waveguide, and a segment of a circular arc. Definitions are provided in the figure:  $a$  represents the radius of the upper circle,  $O_1$  denotes the center of the upper circle,  $d$  is the width of the rectangular bar,  $r$  is the radius of the inner circle of the following arc,  $R$  represents the radius of the outer circle where  $R-r$  equals  $d$ , and the arc's angle is  $2\varphi$ . Here,  $g$  signifies the gap between the inverted rectangular waveguide and the Anchor-like, while  $w$  denotes the width of the waveguide. Additionally,  $l$  represents the distance between the lowest point of the upper circle and the lowest point of the inner circle of the arc, and the height of each individual rectangular bar is denoted by  $h$ .

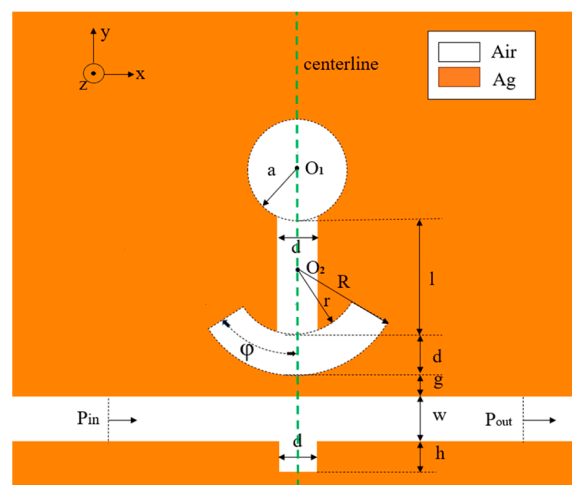


**Figure 1.** Two-dimensional plan of the overall structure.

Electromagnetic waves propagating along the metal–dielectric interface can be categorized into the two following basic modes according to the orientation of the electric and magnetic fields relative to the direction of propagation: transverse electric (TE) and transverse magnetic (TM) modes. In the TE mode, the electric field vector is completely transverse and perpendicular to both the direction of propagation and the metal–dielectric interface. Given that the electric field lacks a component parallel to the metal surface, it fails to effectively interact with the metal's free electrons, thereby failing to excite surface

plasmon polaritons (SPPs). Conversely, in the TM mode, the magnetic field vector is transverse to the direction of propagation, and the electric field includes a component along the interface. This electric field component can interact with the metal surface’s free electrons, inducing their collective oscillations and thereby exciting SPPs [32,33]. Therefore, our analysis concentrates on the TM mode, specifically investigating the relationship between surface plasmon polaritons (SPPs) and dispersion within this context [34]:

$$\tanh(k\omega) = -\frac{2k\alpha_c}{k^2 + p^2\alpha_c} \tag{1}$$

where  $k$  is the wave vector in the waveguide,  $P = \epsilon_{in}/\epsilon_m\alpha_c = [k_0^2 \times (\epsilon_{in} - \epsilon_m) + k]^2$ ,  $\epsilon_{in}$  and  $\epsilon_m$  are the dielectric constants of the dielectric and the metal, respectively, and  $p$  is the ratio of the permittivity  $\epsilon_{in}$  to the metal’s permittivity, and  $k_0 = 2\pi/\lambda_0$  is the free space wave vector.

A key design factor for metal–insulator–metal (MIM) waveguides involve the width of the dielectric layer ( $d$ ). This dimension crucially affects the supported mode types and their levels of confinement. By matching the dielectric layer’s width with the waveguide’s ( $w$ ), specifically at 50 nanometers, the design optimizes the transverse magnetic (TM) mode propagation conditions. It also aims to reduce or eliminate the transverse electric (TE) mode.

In Figure 1, the yellow area represents silver, while the white part represents air. Silver was chosen as the filler metal for the following reasons: among all metallic elements, silver (Ag) has the smallest damping constant and is the best choice for performance at optical frequencies [35], and silver is characterized by a high field strength and low system power; the properties of nanostructured silver make it the most suitable for next-generation plasmonic. We can prepare silver by achieving full deposition on the substrate using the chemical vapor deposition (CVD) and obtain the desired structure through electron beam etching [36]. Considering that the dielectric constant of metallic materials varies with incident frequency, the dielectric constant of silver is modeled using the Drude–Debye approach (assuming a dielectric constant of 1 for air):

$$\epsilon(\omega) = \epsilon_\infty + \frac{\epsilon_s - \epsilon_\infty}{1 + i\omega\tau} + \frac{\sigma}{i\omega\epsilon_0} \tag{2}$$

The parameter values are defined as follows: infinite frequency relative permittivity  $\epsilon_\infty$  equals 3.8344, static dielectric strength  $\epsilon_s$  is  $-9530.5$ , relaxation time  $\tau$  is set at  $7.4 \times 10^{-15}$  s, conductivity  $\sigma$  amounts to  $1.1486 \times 10^7$  s/m, and  $\omega$  represents the angular frequency of light at  $1.38 \times 10^{16}$  rad/s.

This study will evaluate the sensor’s performance using three parameters: FWHM, sensitivity ( $S$ ), and figure of merit (FOM). Sensitivity is crucial for assessing sensor performance. Fano resonance-based MIM waveguide structures detect changes in desired physical quantities by observing variations in wavelength position. In general, sensitivity is defined as follows [37]:

$$S = \frac{\Delta\lambda}{\Delta n} \tag{3}$$

Here,  $\Delta\lambda$  represents changes in refractive index, while  $\Delta n$  denotes changes in wavelength. Fano resonance manifests a distinctive feature in the transmission spectrum; the sharper the curve, the better the performance. We employ the full width at half maximum (FWHM) to characterize the spectrum’s sharpness, specifically, the width of the spectrum at half the height of the resonance peak, which is expressed as follows [38]:

$$\text{FWHM} = \lambda_1 - \lambda_2 \tag{4}$$

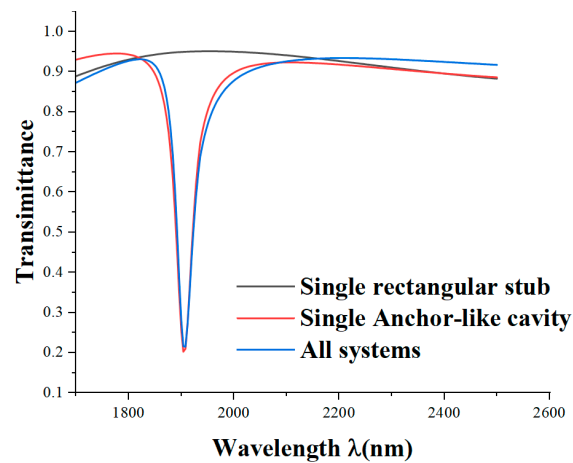
Here, Transmittance at  $\lambda_1$  and  $\lambda_2$  is  $(T_{max} + T_{min})/2$ .  $T_{max}$  and  $T_{min}$  represent the maximum and minimum transmittance in the transmission spectrum. The figure of merit

(FOM) is a crucial parameter for assessing sensors based on MIM waveguide structures and is defined as follows [39]:

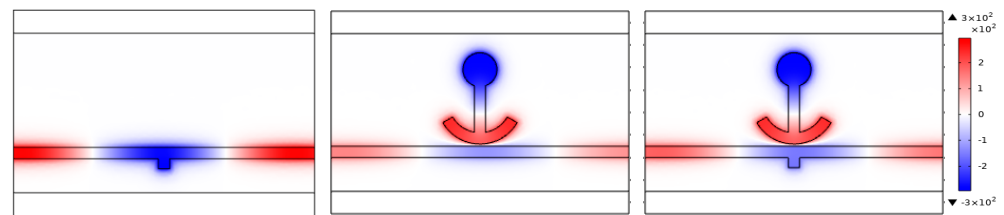
$$FOM = S/FWHM. \tag{5}$$

### 3. Simulation Results and Analysis

We employ COMSOL Multiphysics 5.4a software and a 2D modeling and analysis approach to investigate the frequency domain behavior of electromagnetic waves within the RF module. We focus on frequency domain analysis and boundary mode analysis as the subjects of our study. The 2D model is analyzed through simulation, and the geometric model of the designed sensor system is constructed. We establish the boundary absorption condition as a perfectly matched layer and utilize a free-profile triangular mesh along with hyper-refinement for mesh refinement in the waveguide and Anchor-like structure regions. Mesh refinement for other regions is performed using regularization. This strategy minimizes superfluous computations and upholds calculation precision. Initially, we begin by defining the various parameters of the sensor, the  $r = 140$ ,  $R = 190$ ,  $a = 75$ ,  $d = h = w = 50$  nm,  $l = 195$  nm,  $g = 10$  nm, and  $\varphi = 60^\circ$ . Figure 2 displays the spectrograms of a single rectangular stub, all systems, and a single Anchor-like structure. These are represented by black, red, and blue curves, respectively. The wavelength range spans from 1700 nm to 2500 nm with 1 nm increments.



(a)



(b)

**Figure 2.** (a) Transmission spectra of single rectangular stub, all systems, and a single Anchor-like structure. (b) Magnetic field distribution for different structures.

Spectral analysis reveals that the single anchor structure demonstrates low transmittance and a relatively symmetric shape, indicating a narrow-band mode directly excited by the incident light. Conversely, the transmission spectral profile of the single reverse waveguide structure displays a positive slope with high transmittance, implying a continuous broadband mode. Similarly, the transmission spectrum of a single rectangular stub, with its slightly upward-sloping curve and high transmittance for most optical signal frequencies, exhibits continuous broadband transmission characteristics, this phenomenon is classified

as a continuous broadband mode. The structure reveals an asymmetric curve, signifying the clear presence of a Fano resonance. This phenomenon arises from the interaction between the continuous broadband states generated by the rectangular waveguide and the discrete narrowband states associated with each anchor-like structure, resulting in a significant Fano resonance. This phenomenon arises from the interaction between the anchor-like structures. Additionally, we investigated the effect of refractive index variation on the sensing performance of the designed structure.

Refractive indices ranging from  $n = 1.00$  to  $n = 1.05$  RIUs were simulated with constant structural parameters, as illustrated in Figure 3a. With an increase in refractive index, the transmission spectrum exhibits an almost equidistant red shift. However, the change in refractive index does not alter the waveform of the transmission spectrum; it only shifts its position. Figure 3b demonstrates a linear correlation between the wavelength and the refractive index, indicating the potential use of the proposed structure as a refractive index sensor. Through linear regression analysis to calculate the slope, the sensitivity of this sensor is determined to be 2440 nm/RIU, and the FOM is 63.

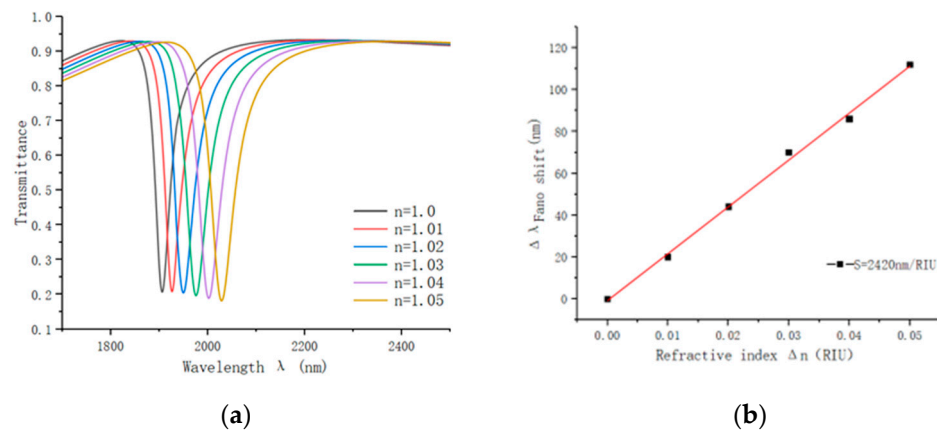


**Figure 3.** (a) Transmittance spectrum at different refractive indices and (b) sensitivity fitting curve.

We discovered that the refractive index is only one factor influencing the Fano resonance, while the specific parameters of the structure can also significantly affect it as well. To delve deeper into the impact of these specific parameters, we initially adjusted the radius size, denoted as ‘a’, while keeping the center of circle  $O_1$  fixed. The radius range was set from 75 to 95 nm in steps of 5 nm, while all other structural parameters remained constant. The transmission spectra and sensitivity curves are illustrated in Figure 4. Subsequently, we explored the influence of another parameter, ‘l’, on the sensor’s propagation performance. Maintaining the distance between the lower arc and the waveguide constant, we shifted the upper circle relatively upward. The parameter ‘l’ varied from 195 nm to 235 nm with a step size of 10 nm, and the other parameters remained unchanged. Figure 5 shows the simulation results.

The results above indicate a continuous redshift in the transmission spectrum as the radii  $a$  and  $l$  increase, accompanied by minor fluctuations in transmittance and FWHM. Additionally, we conducted linear fitting on resonance curves for various radii. As depicted in Figure 4b, sensor sensitivity increases with larger radii  $a$  and  $l$ . Notably, the impact of  $a$  and  $l$  on sensor sensitivity is essentially identical. The maximum sensitivities are 2840 and 2980, respectively, for  $a = 95$  and  $l = 195$  nm.

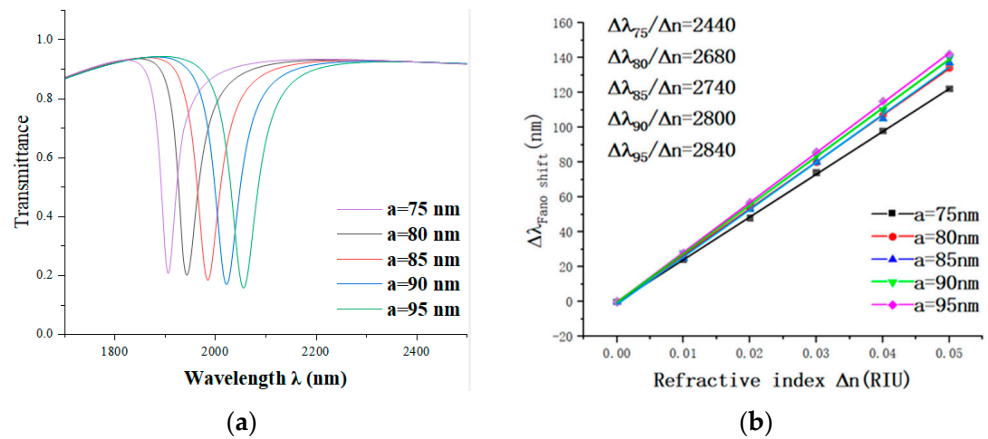


**Figure 4.** (a) The transmittance spectra for radii ranging from 75 to 95 nm. (b) The sensitivity fitting curves for different radii  $a$ .

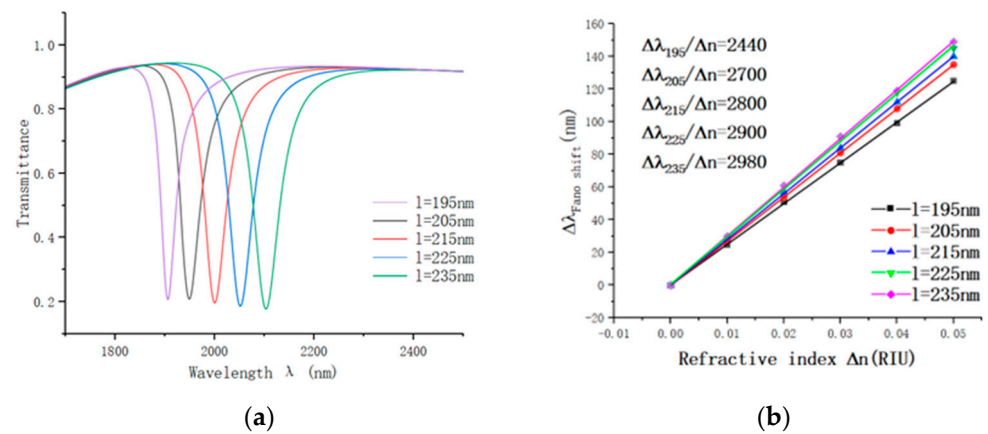


**Figure 5.** (a) The transmittance spectra for  $l$  ranging from 195 to 235 nm. (b) The sensitivity fitting curves for different  $l$ .

To delve deeper into the factors impacting sensor accuracy and to analyze the impact of the coupling gap on sensor performance, we vary the gap between the system and the anchor-like structure. We incrementally increased the coupling gap from 10 nm to 50 nm. As depicted in Figure 6a, the curve noticeably blueshifts, and in Figure 6c, we can see that FWHM significantly narrows with an increasing  $g$ . Additionally, Fano resonance curves are presented in Figure 6a. The increasing transmittance of the Fano resonance curve indicates a notable deterioration in coupling performance, leading to a sharp decline in sensor performance. The sensitivity fitted line for various coupling gaps is illustrated in Figure 6b. The most substantial sensitivity decrease occurs as  $g$  increases from 10 to 20. When  $g$  exceeds 10, the rate of change in sensor sensitivity decreases. However, when  $g$  is less than or equal to zero, implying direct contact between the two structures, the coupling effect becomes exceedingly strong, potentially inducing highly nonlinear behavior. Thus,  $g = 10$  nm emerges as the optimal parameter for this design, corresponding to a sensitivity of 2440 nm/RIU and an FOM of 63.

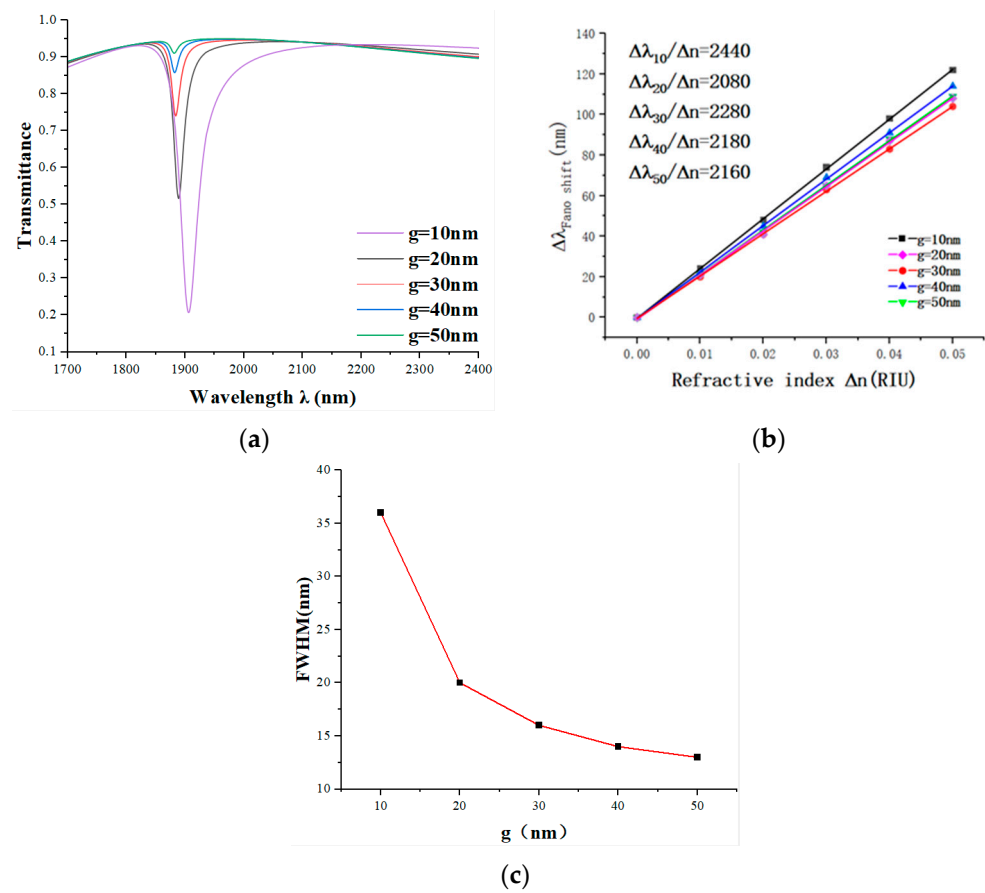


**Figure 6.** (a) The transmittance spectra for  $g$  ranging from 10 to 50 nm, (b) the sensitivity fitting curves for different  $g$ , and (c) the trend of FWHM change.

To assess the impact of changing the height of the reverse rectangular baffle on the sensor’s transmission performance, we incrementally raise it from 45 nm to 85 nm in 10 nm increments while keeping other parameters constant. The simulation results are depicted in Figure 7.

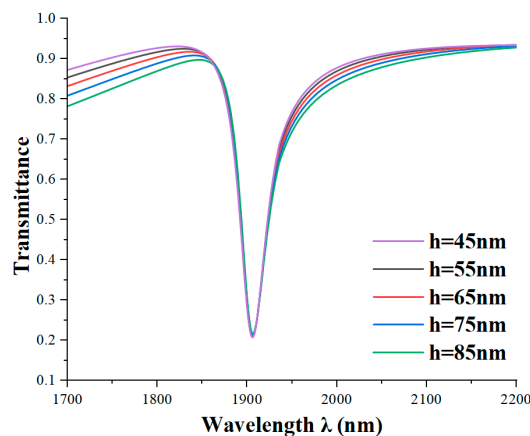


**Figure 7.** The transmittance spectra for  $h$  ranging from 45 to 85 nm.

Regardless of the variation in the height of the inverse rectangle, the position and transmittance of the Fano resonance remain largely stable. Furthermore, the Fano resonance curve exhibits distinct asymmetric features that become more pronounced by increasing the baffle height of the inverse rectangle. Finally, we explore the impact of the arc angle on the sensor’s transmission characteristics, maintaining all other parameters constant while incrementally increasing the arc angle  $\varphi$  from  $60^\circ$  to  $80^\circ$  and  $2\varphi$  from  $120^\circ$  to  $160^\circ$ .

As shown in Figure 8a, as the angle  $2\varphi$  increases from  $120^\circ$  to  $160^\circ$ , a redshift occurs in the transmission spectrum, signifying an increase in the wavelength of transmitted light. At the same time, as shown in Figure 8b, the sensor’s sensitivity undergoes a notable improvement. This indicates that within this angle range, enhancing the angle directly improves the sensor’s performance. However, upon exceeding  $120^\circ$ , the rate of improvement starts to decline, showing that beyond a specific threshold angle, further angle increases result in a gradual reduction in the enhancement of sensor sensitivity.

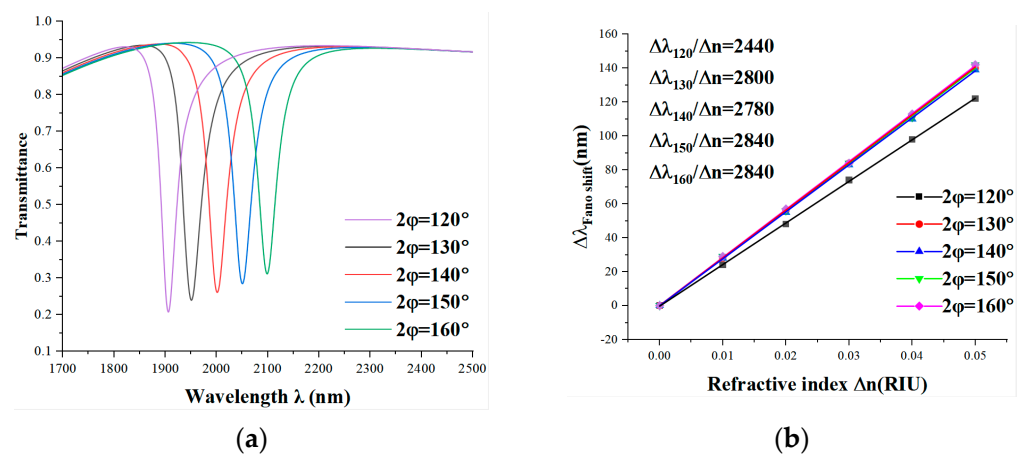


**Figure 8.** (a) The transmittance spectra for  $2\varphi$  ranging from  $120^\circ$  to  $160^\circ$ , (b) the sensitivity fitting curves for different  $2\varphi$ .

Subsequently, we explored the effects of adjusting the angle  $2\varphi$  to  $360^\circ$  and setting  $l$  to 55 to form a ring. This was compared to merely adjusting  $l$  to 55. According to Figure 9a, adjusting  $l$  alone results in a smooth curve and exhibits high transmittance. When  $l$  is set to 55, forming a ring, and compared to only adjusting  $l$  to 55, the figure shows that adjusting  $l$  alone results in a transmission spectrum that becomes a smooth curve with high transmittance. This study further reveals that decreasing the length of  $l$  reduces the sensor’s sensitivity. However, with  $l$  at 55 and arc  $2\varphi$  at  $360^\circ$ , forming a circle that encompasses the inner circle, transmittance decreases. Nonetheless, the arc’s completeness partially compensates for the reduction in transmittance. From the figure, we can also see that the magnetic field distributions of the two different structures are opposite. From Figure 9b,c, we can also see that the magnetic field resonances of the two different structures are opposite. This suffices to demonstrate that the arc’s completeness is a significant factor influencing transmittance at a wavelength of 2082 nm.

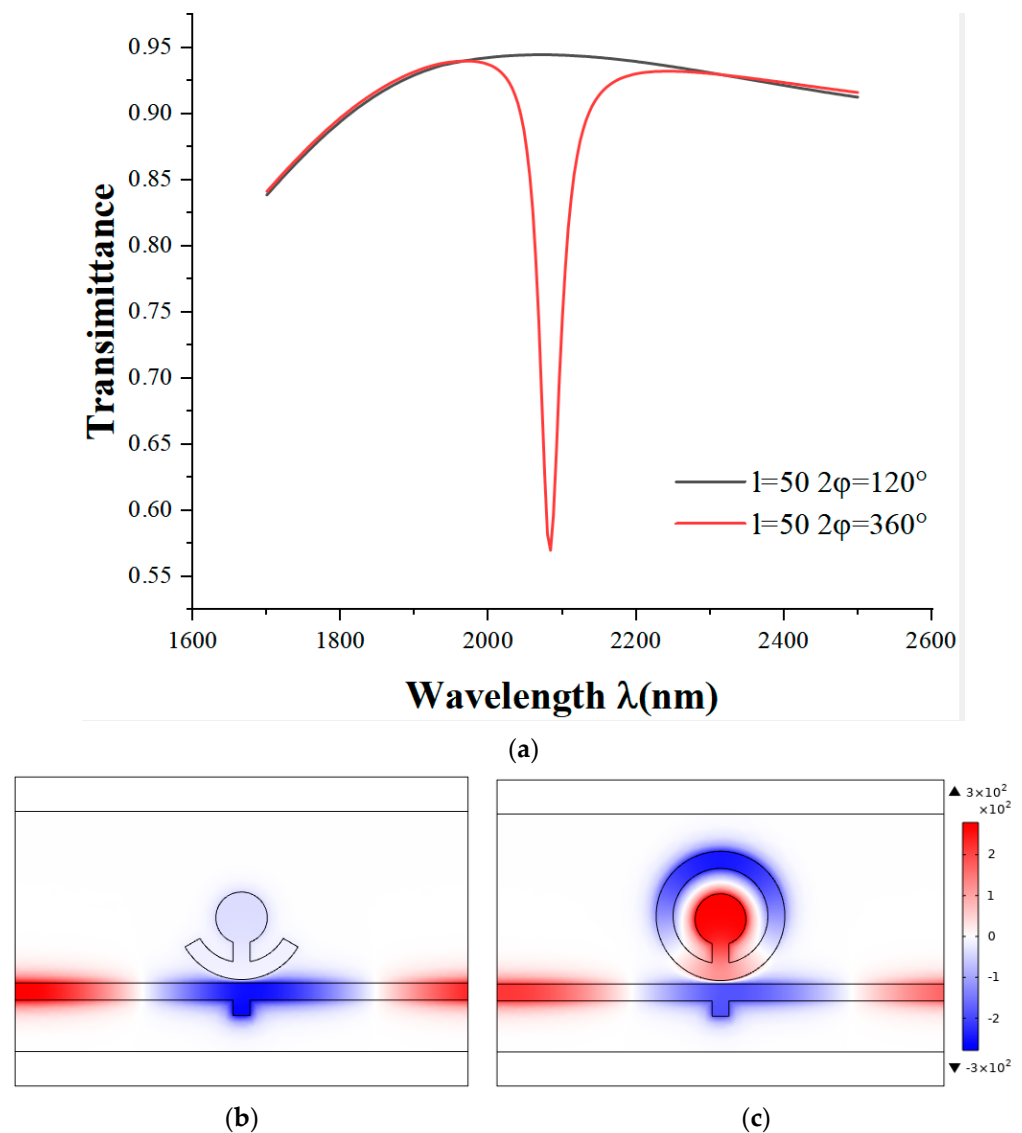


**Figure 9.** (a) The transmission spectra for  $l$  being the same, with  $2\phi$  values of  $120^\circ$  and  $160^\circ$ . (b) The distribution of the magnetic field at a wavelength of 2082 nm when  $2\phi$  is  $120^\circ$ . (c) The distribution of the magnetic field at a wavelength of 2082 nm when  $2\phi$  is  $160^\circ$ .

#### 4. The Application of this Structure in Hemoglobin Concentration

Red blood cells (RBCs) are often crucial indicators of related disorders. Erythrocytes, major blood cells, carry oxygen and carbon dioxide. In clinical practice, they serve as key indicators in routine blood tests, reflecting the body’s RBC production and aiding in diagnosing blood disorders. Hemoglobin (Hb), a special protein in RBCs, transports oxygen. Hemoglobin reference values differ by gender and age: men: 120–165 g/L, women: 110–150 g/L, newborns: 180–190 g/L, and children: 120–140 g/L (12–14 g/dL). Hemoglobin levels in newborns decrease with age, approaching adult levels. Slightly lower hemoglobin is normal in the elderly, during menstruation, or in mid-to-late pregnancy. Chemotherapy, HIV treatment, and conditions such as iron deficiency anemia, aplastic anemia, or thalassemia can reduce red blood cell production or increase loss or destruction, leading to low hemoglobin. Pathological factors such as severe vomiting, diarrhea, extensive burns, and conditions like chronic hypoadrenocorticism, uremia, or renal and hepatic cancer can result in high hemoglobin levels. Monitoring hemoglobin concentration allows for the immediate diagnosis of blood diseases and timely treatment, holding great clinical significance.

The relationship between Hb concentration and RI is defined as follows [40]:

$$n = 1.38 + \frac{H - H_{\text{normal}}}{5766.5} \tag{6}$$

where  $H_{\text{normal}}$  is 140 g/L,  $H$  represents the concentration to be measured, the test range spans from 0 to 300 g/L, and the step size is set at 60 g/L. The detection process entails injecting blood with varied hemoglobin concentrations into the sensor chamber, altering the medium’s refractive index. This results in spectral displacement. Sensor sensitivity is determined by the following equation:

$$S_H = \frac{\Delta\lambda}{\Delta H} \tag{7}$$

where  $\Delta\lambda$  represents the spectrum’s shift and  $\Delta H$  indicates changes in the concentration of blood red cells. Output spectra at various concentrations are depicted in Figure 10a. The resonance trough’s wavelength changes in proportion to Hb concentration increases, with resonance wavelength spacing being 36 nm. The sensor sensitivity fitting is shown in Figure 10b. The sensor sensitivity’s linear fit correlation coefficient exceeds 0.99, the sensor’s sensitivity is 0.6 nm·g/L, and the commercial spectral analyzer’s minimum resolution is 0.001 nm. The sensor provides more accurate concentration measurements than traditional spectroscopic or colorimeter methods. Compared with demand-labeled assay techniques (e.g., enzyme-linked immunosorbent assay—ELISA), a label-free assay is provided with fewer preprocessing steps [41], demonstrating significant potential for advancing high-precision nanoscale hemoglobin concentration monitoring. However, surface plasma sensors are sensitive to ambient temperatures. Prolonged use in a clinical setting may place higher demands on the device’s durability and stability. Ensuring that the device maintains high performance and accuracy over repeated use may be a substantial obstacle for applications requiring large-scale screening, such as routine hemoglobin testing [42].

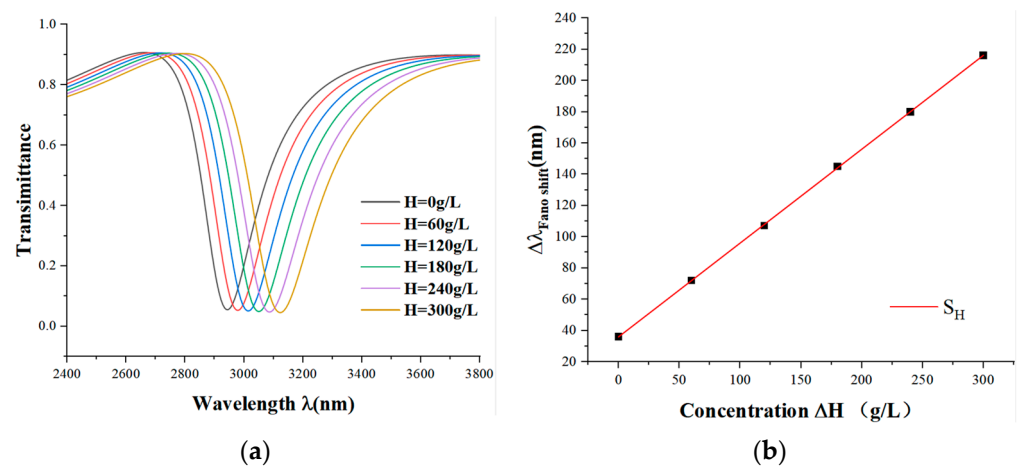


Figure 10. (a) The transmittance spectra for H ranging from 0 to 300 g/L. (b) The sensitivity fitting curve of hemoglobin concentration changes.

### 5. Conclusions

This study introduces a nanoscale refractive index sensor that leverages the unique properties of optical Fano resonance and plasma waveguide coupling. The sensor design combines a MIM waveguide structure with an anchor-like configuration, maximizing the benefits of optical Fano resonance and plasma waveguide coupling. Through finite element analysis, the propagation properties of the composite structure were explored, leading to the development of a novel nanoscale refractive index sensor. Subsequently, the anchor-like structure’s parameters were adjusted to examine their impact on sensor performance, particularly in relation to spectrum transmittance and refractive index changes. By increasing

radius  $a$  and length  $l$ , it is possible to alter the Fano resonance wavelength, thereby enhancing the sensor's performance. Furthermore, enlarging the coupling gap induces a blue shift, which further refines performance. Consequently, this also boosts the Fano resonance curve's transmittance. Modifying the rectangular baffle's height alters the Fano resonance curve's shape without affecting the trough's wavelength. The arc angle  $\varphi$  significantly influences the transmittance. Adjusting this structure's variables may be essential for specific applications to identify the sensor's optimal manufacturing parameters. Additionally, the sensor can detect blood's red blood cell concentration, and the sensor's sensitivity is  $0.6 \text{ nm}\cdot\text{g/L}$ , which can provide some basis for clinical medicine. Moreover, the varying concentration of red blood cells in different blood types enables the differentiation between them, which is foundational for nanosensor research in biomedical and clinical medicine.

**Author Contributions:** Conceptualization, S.Y. and W.J.; methodology, W.J.; software, Y.C.; validation, S.Y., Y.S. and C.Z.; formal analysis, W.J. and Y.Z.; investigation, W.J.; data curation, W.J. and T.W.; writing—original draft preparation, W.J.; writing—review and editing, Y.S. and C.W.; visualization, G.G. and X.M.; supervision, S.Y.; project administration and funding acquisition, S.Y. All authors have read and agreed to the published version of the manuscript.

**Funding:** The author(s) declare financial support was received for the research, authorship, and/or publication of this article. This work was supported in part by the National Natural Science Foundation of China under Grant No. 62374148, in part by the Zhejiang Provincial Natural Science Foundation of China under Grant No. LD21F050001, the Key Research Project by Department of Water Resources of Zhejiang Province under Grant No. RA2101, the Key Research and Development Project of Zhejiang Province under Grant No. 2021C03019, and the Funds for Special Projects of the Central Government in Guidance of Local Science and Technology Development under Grant No. YDZJSX20231A031.

**Institutional Review Board Statement:** Not applicable.

**Informed Consent Statement:** Not applicable.

**Data Availability Statement:** The data provided in this study are available upon request from the corresponding author.

**Acknowledgments:** The authors are grateful to their other colleagues in the laboratory for their understanding and help. They also thank the affiliates for providing the research platform and the sponsors for financial support.

**Conflicts of Interest:** The authors declare no conflicts of interest.

## References

1. Zhao, Y.; Shen, J.-C.; Liu, Q.; Zhu, C.-L. Optical fiber sensor based on helical Fibers: A review. *Measurement* **2022**, *188*, 110400. [[CrossRef](#)]
2. Hu, C.; Shi, Y.; Zhou, T.; Xu, C.; Zhu, A. A small size on-chip temperature sensor based on a microring resonator. *Silicon* **2021**, *14*, 5847–5854. [[CrossRef](#)]
3. Hu, Y.; Tian, Z.; Ma, D.; Qi, C.; Yang, D.; Huang, S. Smart colloidal photonic crystal sensors. *Adv. Colloid Interface Sci.* **2024**, *324*, 103089. [[CrossRef](#)]
4. Zhu, J.; Wu, C. Optical refractive index sensor with Fano resonance based on original MIM waveguide structure. *Results Phys.* **2021**, *21*, 103858. [[CrossRef](#)]
5. Chen, J.-H.; Wang, L.; Feng, Y.-T.; Chen, J.-X.; Zeng, Y.-P. A nano-refractive index sensor based on a MIM waveguide with a semicircular ring rectangular resonator. *Micro Nanostructures* **2024**, *186*, 207730. [[CrossRef](#)]
6. Shan, H.; Zu, S.; Fang, Z. Research Progress in Ultrafast Dynamics of Surface Plasmon Hot Electrons. *Laser Optoelectron. Prog.* **2017**, *54*, 30002. [[CrossRef](#)]
7. Zhang, J.; Zhang, L.; Xu, W. Surface plasmon polaritons: Physics and applications. *J. Phys. D Appl. Phys.* **2012**, *45*, 113001. [[CrossRef](#)]
8. Li, T.; Yan, S.; Liu, P.; Zhang, X.; Zhang, Y.; Shen, L.; Ren, Y.; Hua, E. A nanoscale structure based on an MIM waveguide coupled with a Q resonator for monitoring trace element concentration in the human body. *Micromachines* **2021**, *12*, 1384. [[CrossRef](#)] [[PubMed](#)]
9. Schuller, J.A.; Barnard, E.S.; Cai, W.; Jun, Y.C.; White, J.S.; Brongersma, M.L. Plasmonics for extreme light concentration and manipulation. *Nat. Mater.* **2010**, *9*, 193–204. [[CrossRef](#)]
10. Barnes, W.L.; Dereux, A.; Ebbesen, T.W. Surface plasmon subwavelength optics. *Nature* **2003**, *424*, 824–830. [[CrossRef](#)]

11. Pérez-Ocón, F.; Pozo, A.M.; Cortina, J.; Rabaza, O. Design of a Surface Plasmon Resonance CO Sensor. *Sensors* **2022**, *22*, 3299. [[CrossRef](#)] [[PubMed](#)]
12. Vahedi, A.; Kouhi, M. Liquid crystal-based surface plasmon resonance biosensor. *Plasmonics* **2020**, *15*, 61–71. [[CrossRef](#)]
13. Mahmoudpour, M.; Dolatabadi, J.E.N.; Torbati, M.; Homayouni-Rad, A. Nanomaterials based surface plasmon resonance signal enhancement for detection of environmental pollutions. *Biosens. Bioelectron.* **2019**, *127*, 72–84. [[CrossRef](#)] [[PubMed](#)]
14. Fang, M.; Shi, F.; Chen, Y. Unidirectional all-optical absorption switch based on optical Tamm state in nonlinear plasmonic waveguide. *Plasmonics* **2016**, *11*, 197–203. [[CrossRef](#)]
15. Wei, D.; Hu, C.; Chen, M.; Shi, J.; Luo, J.; Zhang, X.; Wang, H.; Xie, C. Optical modulator based on the coupling effect of different surface plasmon modes excited on the metasurface. *Opt. Mater. Express* **2020**, *10*, 105–118. [[CrossRef](#)]
16. Fang, Y.; Sun, M. Nanoplasmonic waveguides: Towards applications in integrated nanophotonic circuits. *Light. Sci. Appl.* **2015**, *4*, e294. [[CrossRef](#)]
17. Chandran, A.; Barnard, E.S.; White, J.S.; Brongersma, M.L. Metal-dielectric-metal surface plasmon-polariton resonators. *Phys. Rev. B* **2012**, *85*, 085416. [[CrossRef](#)]
18. Dai, M.; Chen, Z.; Zhao, Y.; Gandhi, M.S.A.; Li, Q.; Fu, H. State-of-the-art optical microfiber coupler sensors for physical and biochemical sensing applications. *Biosensors* **2020**, *10*, 179. [[CrossRef](#)]
19. Li, X.; Gu, Y.; Luo, R.; Wang, L.; Gong, Q. Effects of dielectric anisotropy on surface plasmon polaritons in three-layer plasmonic nanostructures. *Plasmonics* **2013**, *8*, 1043–1049. [[CrossRef](#)]
20. Veronis, G.; Fan, S. Crosstalk between three-dimensional plasmonic slot waveguides. *Opt. Express* **2008**, *16*, 2129–2140. [[CrossRef](#)]
21. Rahmatiyar, M.; Afsahi, M.; Danaie, M. Design of a refractive index plasmonic sensor based on a ring resonator coupled to a MIM waveguide containing tapered defects. *Plasmonics* **2020**, *15*, 2169–2176. [[CrossRef](#)]
22. Qin, M.; Zhai, X.; Wang, L.; Li, H.; Xia, S.; Lin, Q.; Zhang, B. Double Fano resonances excited in a compact structure by introducing a defect. *EPL* **2016**, *114*, 57006. [[CrossRef](#)]
23. Hu, F.; Chen, F.; Zhang, H.; Sun, L.; Yu, C. Sensor based on multiple Fano resonances in MIM waveguide resonator system with silver nanorod-defect. *Optik* **2021**, *229*, 166237. [[CrossRef](#)]
24. Yang, Q.; Liu, X.; Guo, F.; Bai, H.; Zhang, B.; Li, X.; Tan, Y.; Zhang, Z. Multiple Fano resonance in MIM waveguide system with cross-shaped cavity. *Optik* **2020**, *220*, 165163. [[CrossRef](#)]
25. Wang, Y.; Huo, Y.; Cui, P.; Song, M.; Zhao, C.; Liao, Z.; Liu, T.; Zhang, Z.; Xie, Y. Ultrahigh FOM and multiple Fano resonances in MIM waveguide systems with half-ring and rectangular cavities. *J. Comput. Electron.* **2023**, *22*, 839–848. [[CrossRef](#)]
26. Pang, S.; Huo, Y.; Xie, Y.; Hao, L. Fano resonance in MIM waveguide structure with oblique rectangular cavity and its application in sensor. *Opt. Commun.* **2016**, *381*, 409–413. [[CrossRef](#)]
27. Zhou, C.; Huo, Y.; Guo, Y.; Niu, Q. Tunable multiple fano resonances and stable plasmonic band-stop filter based on a metal-insulator-metal waveguide. *Plasmonics* **2021**, *16*, 1735–1743. [[CrossRef](#)]
28. Tathfif, I.; Rashid, K.S.; Yaseer, A.A.; Sagor, R.H. Alternative material titanium nitride based refractive index sensor embedded with defects: An emerging solution in sensing arena. *Results Phys.* **2021**, *29*, 104795. [[CrossRef](#)]
29. Tang, Y.; Zhang, Z.; Wang, R.; Hai, Z.; Xue, C.; Zhang, W.; Yan, S. Refractive index sensor based on Fano resonances in metal-insulator-metal waveguides coupled with resonators. *Sensors* **2017**, *17*, 784. [[CrossRef](#)]
30. Chen, J.-H.; Chen, J.-H.; Wang, L.; Wang, L.; Chen, J.-X.; Chen, J.-X.; Zeng, Y.-P.; Zeng, Y.-P.; Liang, Q.-Q.; Liang, Q.-Q.; et al. A refractive index sensor based on the MIM waveguide with a semi-elliptical and a rectangular ring resonant cavity. *Mod. Phys. Lett. B* **2023**, *37*, 2350141. [[CrossRef](#)]
31. Wang, L.; Zeng, Y.-P.; Wang, Z.-Y.; Xia, X.-P.; Liang, Q.-Q. A refractive index sensor based on an analogy T shaped metal-insulator-metal waveguide. *Optik* **2018**, *172*, 1199–1204. [[CrossRef](#)]
32. Chen, A.T.C.; Rakib Uddin, M. Transverse Electric (TE) and Transverse Magnetic (TM) Modes Dependent Effective Index Analysis for a Nano-scale Silicon Waveguide. In Proceedings of the 2022 24th International Conference on Advanced Communication Technology (ICACT), Pyeongchang, Republic of Korea, 13–16 February 2022.
33. Lee, S.-Y.; Lee, I.-M.; Park, J.; Oh, S.; Lee, W.; Kim, K.-Y.; Lee, B. Role of magnetic induction currents in nanoslit excitation of surface plasmon polaritons. *Phys. Rev. Lett.* **2012**, *108*, 213907. [[CrossRef](#)] [[PubMed](#)]
34. Choi, B.B.; Kim, B.; Bice, J.; Taylor, C.; Jiang, P. Inverse DVD-R grating structured SPR sensor platform with high sensitivity and figure of merit. *J. Ind. Eng. Chem.* **2022**, *116*, 321–330. [[CrossRef](#)]
35. Rakhshani, M.R.; Mansouri-Birjandi, M.A. High sensitivity plasmonic refractive index sensing and its application for human blood group identification. *Sensors Actuators B Chem.* **2017**, *249*, 168–176. [[CrossRef](#)]
36. Höflich, K.; Jurczyk, J.; Zhang, Y.; dos Santos, M.V.P.; Götz, M.; Guerra-Nuñez, C.; Best, J.P.; Kapusta, C.; Utke, I. Direct electron beam writing of silver-based nanostructures. *ACS Appl. Mater. Interfaces* **2017**, *9*, 24071–24077. [[CrossRef](#)] [[PubMed](#)]
37. Liu, N.; Weiss, T.; Mesch, M.; Langguth, L.; Eigenthaler, U.; Hirscher, M.; Sönnichsen, C.; Giessen, H. Planar metamaterial analogue of electromagnetically induced transparency for plasmonic sensing. *Nano Lett.* **2010**, *10*, 1103–1107. [[CrossRef](#)] [[PubMed](#)]
38. Liu, H.; Gao, Y.; Zhu, B.; Ren, G.; Jian, S. A T-shaped high resolution plasmonic demultiplexer based on perturbations of two nanoresonators. *Opt. Commun.* **2015**, *334*, 164–169. [[CrossRef](#)]
39. Kekatpure, R.D.; Hryciw, A.C.; Barnard, E.S.; Brongersma, M.L. Solving dielectric and plasmonic waveguide dispersion relations on a pocket calculator. *Opt. Express* **2009**, *17*, 24112–24129. [[CrossRef](#)] [[PubMed](#)]

40. Yadav, G.K.; Metya, S.K.; Zafar, R.; Garg, A.K. High sensitivity plasmonic refractive index sensor for early anemia detection. *Photonics Nanostructures-Fundam. Appl.* **2024**, *58*, 101235. [[CrossRef](#)]
41. Jaria, G.; Calisto, V.; Otero, M.; Esteves, V.I. Monitoring pharmaceuticals in the aquatic environment using enzyme-linked immunosorbent assay (ELISA)—A practical overview. *Anal. Bioanal. Chem.* **2020**, *412*, 3983–4008. [[CrossRef](#)]
42. You, K.E.; Uddin, N.; Kim, T.H.; Fan, Q.H.; Yoon, H.J. Highly sensitive detection of biological substances using microfluidic enhanced Fabry-Perot etalon-based optical biosensors. *Sensors Actuators B Chem.* **2018**, *277*, 62–68. [[CrossRef](#)]

**Disclaimer/Publisher’s Note:** The statements, opinions and data contained in all publications are solely those of the individual author(s) and contributor(s) and not of MDPI and/or the editor(s). MDPI and/or the editor(s) disclaim responsibility for any injury to people or property resulting from any ideas, methods, instructions or products referred to in the content.